Electrical Conductance of Oxidized Rough Sphere Contacts: A Greenwood-Tripp-Based Model

Vladislav A Yastrebov

Electrical Conductance of Oxidized Rough Sphere Contacts: A Greenwood-Tripp-Based Model

Vladislav A. Yastrebov

Centre des matériaux, Mines Paris - PSL, CNRS UMR 7633, 780000 Versailles, France

Abstract

Electrical conductance of rough contacts is strongly affected by the presence of surface oxides, particularly when oxide films are discontinuous and no clear separation of length scales exists between roughness, oxide morphology, and contact size. In this work, we develop a statistical model for electrical conductance in oxidized rough sphere contacts. Oxide films are represented as spatially heterogeneous insulating regions generated by thresholded Gaussian random fields, allowing controlled variation of oxide coverage and correlation length. Mechanical contact is treated within a Greenwood-Tripp-based formulation, while electrical conductance is evaluated using Greenwood's constriction resistance model applied to the resulting population of *conducting* microcontacts. A comprehensive parametric study reveals the role of oxide morphology and allows to formulate a simple phenomenological model for the average conductance. This new model is in a good agreement with the extended Barber's model.

Keywords: electric contact resistance, conductivity, roughness, contact, oxide films, contact spots, Greenwood-Tripp model, Barber bounds.

Contents

*vladislav.yastrebov@minesparis.psl.eu

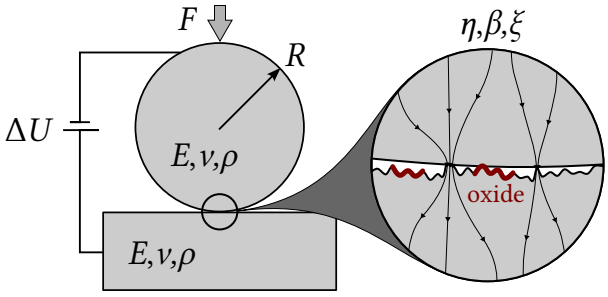

Figure 1: The problem under consideration consists of an elastic sphere of radius R^* brought into contact with an elastic half-space under a normal load P. The effective surface is rough, characterized by an asperity density η and a mean asperity curvature radius β, and is partially covered by insulating oxide films with a surface fraction ξ, randomly distributed over the interface (shown in reddish). An applied electric potential difference ΔU induces an electric current through the oxide-free regions of the contact interface.

1 Introduction

Electrical contact resistance plays a central role in the performance, reliability, and durability of a wide range of engineering systems, from microelectronic devices and electrical connectors to power transmission components and tribological interfaces. It directly governs energy losses, local heating, signal integrity, and, in many cases, the onset of degradation mechanisms. Despite its apparent simplicity, electrical contact resistance is controlled by complex multi-scale phenomena involving surface roughness, real contact area, material properties, and surface films, making it sensitive to mechanical loading and surface condition [Holm, 1967, Timsit, 2014]. A predictive understanding of electrical contact resistance is therefore essential not only for the design of efficient electrical interfaces, but also for advancing the fundamental understanding of coupled mechanical-electrical transport processes at rough contacts.

The mechanics community has developed a mature and quantitative understanding of normal contact between rough surfaces, including how roughness statistics such as asperity density, curvature, and spectral bandwidth control the evolution of the real contact area under load [Müser et al., 2017, Pastewka et al., 2025]. Since the real contact area provides the physical pathways for electrical current, this framework naturally supports models of electrical transport through rough interfaces. In the absence of surface films, the electrical constriction resistance associated with these micro-contacts is well understood, and Barber's rigorous analysis [Barber, 2003] establishes a direct equivalence between normal contact stiffness and electrical (as well as thermal) conductance. However, when insulating oxide films are present at the contact interface, this equivalence breaks down [Persson, 2022]. As a result, the evolution of mechanical contact and electrical conductivity become partially decoupled, and a predictive description requires a separate but coupled analysis of elastic rough contact and the resulting electrical transport problem.

A limited number of studies have addressed oxidized rough contacts using numerical simulations [Lee et al., 2011, Liu et al., 2015]; however, these results remain partial and do not provide a conclusive and quantitative description of the coupled mechanical and electrical behavior.

In this study, we consider the problem of rough contact between a sphere and a nominally flat elastic substrate in the presence of oxide films. The configuration under consideration is illustrated in Fig. 1. The objective of this work is to construct a relatively simple model capable of predicting the combined effects of surface roughness and insulating oxide films on the effective electrical contact resistance.

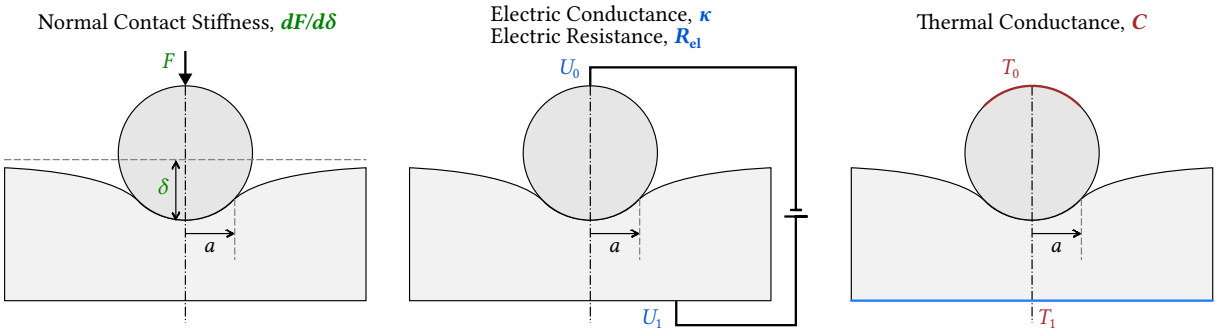

Figure 2: Barber's equivalence relates the normal contact stiffness $K = dF/d\delta$, the electric conductance κ (or equivalently the electric resistance $R_{\rm el} = 1/\kappa$) and the thermal conductance C for the same contact system through the following equation: $K/E^* = \rho^*/R_{\rm el} = C/k^*$, where E^* is the effective elastic modulus, ρ^* the effective electric resistivity, k^* the effective thermal conductivity. This equivalence for the electric resistance holds in the absence of insulating oxide films.

2 Analytical Models

2.1 Stiffness-conductivity equivalence

First, we briefly recall the equivalence between the normal contact stiffness and the electric (or thermal) conductance for half-spaces and finite size systems introduced in [Barber, 2003] and [Sevostianov, 2010, Barber, 2013], respectively, see Fig. 2. Following [Barber, 2003], consider two elastic conductive half-spaces with Young's moduli E_i, Poisson's ratios ν_i, and electric resistivity ρ_i for $i = \{1,2\}$. They come in contact under the action of force F over a compact zone $\mathcal{A}$ and are held at potential $\pm U_0$ at their infinitely remote parts from the contact zone. Then, the resistance $R_{\rm el}$ is inversely proportional to the normal contact stiffness $K(\mathcal{A})$:

$$\frac{1}{R_{\rm el}} = \frac{1}{E^*\rho^*} K(\mathcal{A}), \quad K(\mathcal{A}) = \frac{dF}{d\delta} \tag{1}$$

where E^* is the contact-related effective elastic modulus, ρ^* is the effective resistivity

$$E^* = \frac{E_1 E_2}{(1-\nu_1^2)E_2 + (1-\nu_2^2)E_1}, \qquad \rho^* = \frac{\rho_1 + \rho_2}{2},$$

and δ is the approaching between distant points between two half-spaces. Equivalently, the conductivity κ of the contact interface is proportional to this stiffness :

$$\kappa(\mathcal{A}) = \frac{K(\mathcal{A})}{E^*\rho^*}. \tag{2}$$

The contact stiffness for relatively smooth surfaces depends only on the contact zone $\mathcal{A}$ (its area and its morphology [Beguin and Yastrebov, 2025]) and thus does the electric conductivity.

The simplest example to consider is Hertzian contact between solids of revolution [Johnson, 1987]. For the effective curvature radius R^*, the relation between the contact force F and the approaching of distance points δ is given by

$$F = \frac{4E^*\sqrt{R^*}}{3}\delta^{3/2},$$

which results in the following stiffness

$$K = \frac{dF}{d\delta} = 2E^*\sqrt{R^*\delta} = 2E^* a,$$

where $a = \sqrt{R^*\delta}$ is the contact radius according to the classical Hertz's result. It is important to notice here that the normal elastic stiffness of a flat cylindrical punch of radius a is also $K = 2E^*a$ [Johnson, 1987]. Since we have the elastic stiffness, we can readily obtain the conductivity using Eq. (2) as $\kappa = 2a/\rho^*$, which is the classical results for the potential flow through a circular hole [Helmholtz, 1860, Strutt, 1871] adapted to electric contact in [Holm, 1967].

This very helpful equivalence between the scaled normal stiffness and the conductivity is not applicable if the contact surface has a heterogeneous conductivity and, in the extreme case, if it has insulating or quasi-insulating zones which can be caused by some contamination or presence of insulating oxide films [Timsit, 2014]. The equivalence ceases to work since the contact area is no longer equivalent to conductive area. However, if one knows the fraction of the conductive spots (also called a-spot) forming a subset of the contact area $\mathcal{C} \subset \mathcal{A}$, one can readily formulate bounds on the conductivity under the strong assumption that the fraction of the non-conductive contact set (oxidized/insulating zone) $\mathcal{O} = \mathcal{A} \setminus \mathcal{C}$ to the contact area $\mathcal{A}$ is given by constant $\xi \in [0,1]$[1]:

$$\min_{\substack{\mathcal{C}\subset\mathcal{A} \\ \|\mathcal{O}\|/\|\mathcal{A}\|=\xi}} \{K(\mathcal{C})\} \le \kappa E^* \rho^* \le \max_{\substack{\mathcal{C}\subset\mathcal{A} \\ \|\mathcal{O}\|/\|\mathcal{A}\|=\xi}} \{K(\mathcal{C})\} \tag{3}$$

where min and max are taken over all possible configurations of the conductive zone $\mathcal{C}$ within the contact zone $\mathcal{A}$, and $\|\bullet\|$ denotes the corresponding total area.

2.2 Circular oxidized contact

For a circular contact zone $\mathcal{A}_\circ$ of radius a with the oxide surface fraction ξ, i.e. $\|\mathcal{O}\| = \xi\|\mathcal{A}_\circ\|$ which implies that the conductive zone occupies the area $\|\mathcal{C}\| = (1-\xi)\|\mathcal{A}_\circ\|$, the bounds will consist in a *lower bound* corresponding to a compact circular spot of radius $c = a\sqrt{1-\xi}$ arbitrary located within the contact circle $\mathcal{A}_\circ$ and an *upper bound* corresponding to an annular ring centred at the contact circle with the outer radius equal to a and the inner radius given by $a\sqrt{\xi}$ so $\sqrt{\xi}a \le r \le a$. The conductivity of such an annular ring was estimated in [Love, 1976] as

$$\kappa((1-\xi)\|\mathcal{A}_\circ\|) = f(\xi)\,\kappa(\mathcal{A}_\circ),$$

where $\kappa(\mathcal{A}_\circ)$ is the conductivity of the circular contact and the corrective factor $f(\xi)$ is given by

$$f(\xi) = 1 - \frac{4}{2\pi^2}\xi^{\frac{3}{2}} - \frac{8}{15\pi^2}\xi^{\frac{5}{2}} - \frac{16}{27\pi^2}\xi^3 - \frac{92}{315\pi^2}\xi^{\frac{7}{2}} - \frac{416}{675\pi^2}\xi^4 + o(\xi^4). \tag{4}$$

This estimation remains quite accurate as long as ξ is small (see [Beguin and Yastrebov, 2025]). Hence, for a circular contact with oxide-zone surface fraction ξ, the normalized conductivity $\tilde{\kappa}$ would be "bounded" as

$$\sqrt{1-\xi} \quad \le \quad \tilde{\kappa} \quad \le \quad f(\xi), \qquad \tilde{\kappa} = \frac{\kappa\rho^*}{2a} \tag{5}$$

where, under the assumption of the constant oxide fraction ξ in contact area, the lower bound is exact and the upper one is quite accurate for low values of ξ.

2.3 Extended Barber's bounds

A further layer of difficulty comes from the surface roughness resulting in complex shapes of contact spots and their uneven distribution. In [Barber, 2003], an interesting framework to bound the conductivity of rough contact was constructed. It is based on two force-displacement curves obtained for smooth

[1] Of course, this assumption of constant conductive fraction is too strong, and in the general case, even if over a certain area the oxide fraction is given by ξ, the conductivity of a particular contact would vary between zero (all contact spots are covered by insulating film) and the conductivity of the contact area (none of contact zones is covered by oxides), nevertheless if the characteristic size of oxide islands is much smaller than the contact area, this assumption becomes meaningful.

contact (in absence of small scale roughness) with touch points that differ by the roughness height parameter $s = \max\{z(x,y)\} - \min\{z(x,y)\}$, i.e. the difference between the highest peak and the deepest valley over the potential contact zone. According to Barber's analysis [Barber, 2003, Sect. 6(a)], to get the bounds for the normal stiffness $K_- \le K \le K_+$ and hence for the conductivity $C_\pm$ of a Hertzian contact, the following procedure should be followed. First, the following equation should be solved (see [Barber, 2003, Eq. (6.8)]):

$$S = \tfrac{1}{3}(2x^3 - 3x^2 + 1), \quad x = \sqrt{\frac{\zeta - s}{\zeta_0}}, \quad S = \frac{s}{\zeta_0}, \tag{6}$$

where ζ is the approaching between a sphere and a plane, and ζ_0 is such a value of the approaching that the tangent at the upper force branch (corresponding to the first contact) when intersecting the lower force branch (corresponding to the potential lower contact) corresponds to the applied force F. The positive solutions of this equation are given by

$$x_+(S) = \tfrac{1}{2} + \cos\big(\theta(S)\big), \quad x_-(S) = \tfrac{1}{2} + \cos\big(\theta(S) - \tfrac{2\pi}{3}\big), \quad \theta(S) = \tfrac{1}{3}\arccos(6S-1), \tag{7}$$

but by construction, the unknown $x = \sqrt{(\zeta - s)/\zeta_0}$ depends on ζ_0, so we obtain a transcendent equation. Therefore, a closed form solution seems impossible, and we simply follow Barber's approach: by varying x in the interval $x_+ \in [0,1]$ we obtain the value of S_+ for the upper stiffness bound and by varying $x_- \in [1,\infty]$ we obtain the lower bound S_-, then the normalized force and conductivity are given by

$$F'_\pm = \frac{2F_\pm}{E^*\sqrt{R^* s^3}} = \frac{8}{3}\left(\frac{x_\pm^2}{S_\pm}\right)^{3/2}, \quad \kappa'_\pm = \frac{2\rho^*\kappa}{\sqrt{R^* s}} = \frac{4}{\sqrt{S_\pm}}. \tag{8}$$

Note that the force scales with $\sqrt{R^* s^3}$ and the conductivity with $\sqrt{R^* s}$. This solution is shown in Fig. 3 (with black lines).

By combining in a multiplicative way (8) and (5), we can obtain new bounds taking into account surface roughness handled (implicitly) by parameter s and oxide fraction ξ resulting in the lower and upper bounds given by

$$\kappa'_+ = 4\frac{f(\xi)}{\sqrt{S_+}}, \quad \kappa'_- = 4\sqrt{\frac{1-\xi}{S_-}}, \tag{9}$$

where $f(\xi)$ is given in (4). The generalized p-average of the two bounds can be taken as the first order estimation for the conductance:

$$\langle \kappa' \rangle_p = \left[\frac{1}{2}\left\{\left(4\frac{f(\xi)}{\sqrt{S_+}}\right)^p + \left(4\sqrt{\frac{1-\xi}{S_-}}\right)^p\right\}\right]^{1/p}. \tag{10}$$

This p-average is equivalent to algebraic mean for $p = 1$ and to geometric mean for $p = 0$.

Fig. 3 shows the conductivity accounting for insulating oxide films with surface fraction $\xi \in \{0.3, 0.5, 0.7\}$ (colored solid and dashed curves). As one can see, the presence of oxides expectedly lowers the two bounds compared to the clean-surface case.

It is worth noting that Barber's approach holds an inherent difficulty in defining the key parameter s for the construction of these bounds, which corresponds to the height difference between the highest and the lowest points in contact. First, it is not easy to determine over which zone this parameter should be evaluated. Second, in most practical contact situations the deepest valleys do not come in contact, which introduces an additional ambiguity. Third, for a Gaussian distribution the local difference between the highest and the lowest points can be unboundedly high. Fourth, the scale separation between the roughness and the contact geometry is not always verified in practical applications and if not, the contact clusters appear outside the contact zone predicted by the Hertz theory [Greenwood and Tripp, 1967, Yastrebov, 2019]. And finally, there is no receipt to construct the

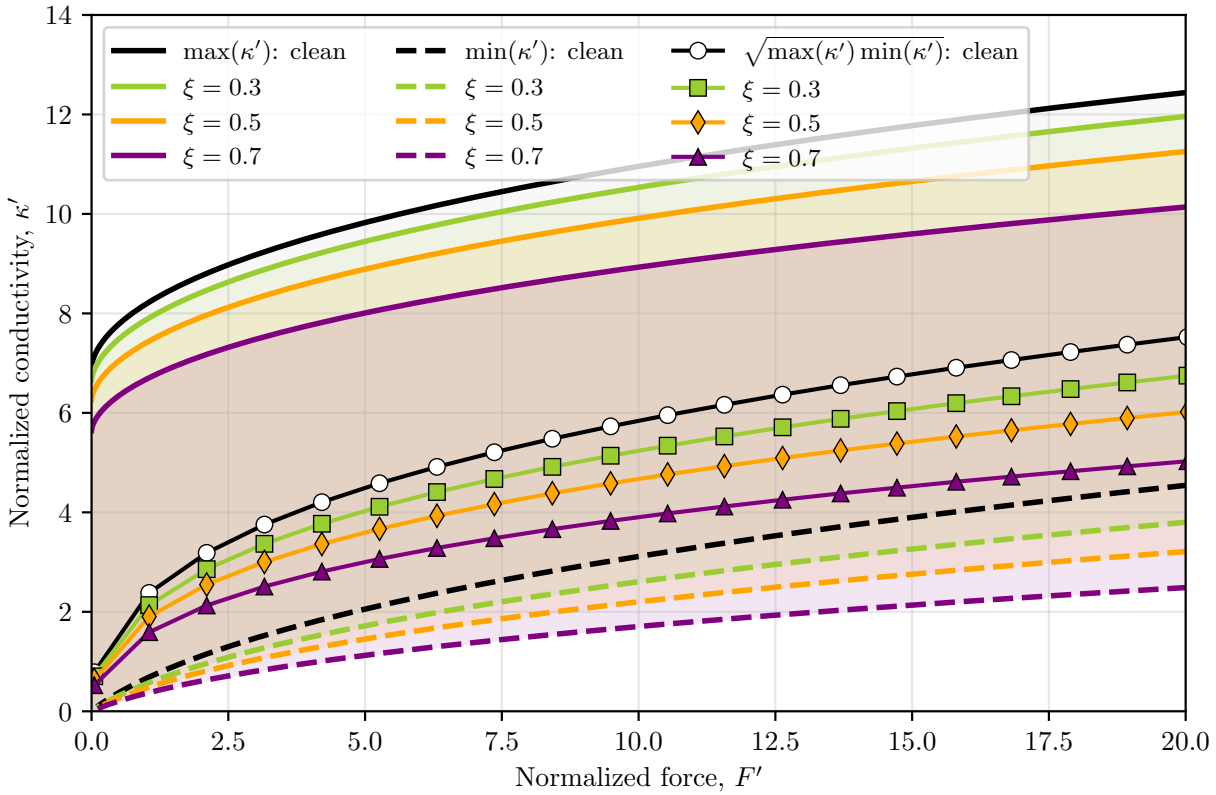

Figure 3: Lower and upper normalized conductivity bounds for Hertzian contact between clean rough surfaces (Eq. (8) from [Barber, 2003]) and with oxide fraction $\xi \in \{0.3, 0.5, 0.7\}$, Eq. (9). The geometric average of the two bounds $\langle \kappa' \rangle_{p=0}$ is also plotted.

average conductivity between the bounds. Nevertheless, the Barber's approach could provide a good indication, and in practical applications, the height parameter s can be replaced by a multiple of the roughness standard deviation $s \sim \mathrm{std}(z)$. If equipped with the adjustment due to oxide-fraction, this approach becomes even more general.

2.4 Extended Greenwood's model

Let us consider a Hertzian contact (or any other contact geometry with a single macro cluster of contacts): there is a localized macroscopic zone containing all individual microscopic contact zones (scale 1), this contact cluster results in a macroscopic current restriction corresponding to resistance R_i. On the smaller scale, every individual contact spot results in its own local current restriction (scale 2). The total resistance due to individual contact spots is given as an inverse of their total conductivity $R_p = 1/\sum_i \kappa_i$ which for circular spots of radii a_i results in

$$R_p = \frac{\rho^*}{2\sum a_i}.$$

The sum of two current restriction result in the total contact resistance

$$R_c = R_p + R_i. \tag{11}$$

According to [Greenwood, 1966], the resulting macroscopic constriction resistance can be computed as

$$R_i = \frac{\rho^*}{\pi} \frac{\sum\limits_{i,i\neq j}\sum\limits_{j} a_i a_j/d_{ij}}{(\sum\limits_i a_i)^2}, \tag{12}$$

where d_{ij} is the distance between centres of contact spots i and j. This equation in a compact form can we written as

$$R_i = \frac{\rho^*}{2\alpha_{\mathrm{HG}}}, \qquad \alpha_{\mathrm{HG}} = \frac{\pi}{2} \frac{(\sum\limits_i a_i)^2}{\sum\limits_{i,i\neq j}\sum\limits_{j} a_i a_j/d_{ij}}, \tag{13}$$

where α_{HG} is the Holm-Greenwood resistance radius [Holm, 1967, Greenwood, 1966].

This equation can include a fraction of insulating oxide films by assuming that only a fraction $1-\xi$ of contact spots $i \in \mathcal{C} \subset \mathcal{A}$ conducts electricity. We can assume that every spot has a state $\phi_i \in \{0,1\}$: when $\phi_i = 1$ the spot is active, if $\phi_i = 0$ - inactive; the variable ϕ follows Bernoulli probability, the probability is $(1-\xi)$ for a spot to be active and ξ to be inactive. Then the self-resistance and its average value are given by

$$R_p(\xi) = \frac{\rho^*}{2\sum \phi_i a_i}, \qquad \langle R_p(\xi)\rangle = \frac{\rho^*}{2(1-\xi)\sum a_i}, \tag{14}$$

and the interaction term takes the following form

$$R_i(\xi) = \frac{\rho^*}{2\alpha_{\mathrm{HG}}(\xi)}, \qquad \alpha_{\mathrm{HG}}(\xi) = \frac{\pi}{2} \frac{(\sum\limits_i \phi_i a_i)^2}{\sum\limits_{i,i\neq j}\sum\limits_{j} \phi_i\phi_j a_i a_j/d_{ij}}. \tag{15}$$

Equations (14,15) can be used directly to evaluate the resistance of a contact area covered by a partial oxide film of surface fraction ξ. Nevertheless, for the completeness of presentation, we can rigorously demonstrate that the Holm-Greenwood radius should remain unchanged for a multi-spot contact case. It we approximate it as the ratio of the average numerator to the average denominator

$$\langle \alpha_{\mathrm{HG}}(\xi)\rangle \approx \frac{\pi}{2} \frac{\langle (\sum\limits_i \phi_i a_i)^2\rangle}{\left\langle \sum\limits_{i,i\neq j}\sum\limits_{j} \phi_i\phi_j a_i a_j/d_{ij} \right\rangle}.$$

The denominator, in average, simply reduced to

$$\left\langle \sum_{i,i\neq j}\sum_{j}\phi_i\phi_j a_i a_j/d_{ij} \right\rangle = (1-\xi)^2 \sum_{i,i\neq j}\sum_{j} a_i a_j/d_{ij},$$

whereas the average of the numerator can be evaluated as

$$\left\langle \left(\sum_i \phi_i a_i\right)^2 \right\rangle = \left\langle \sum_i \phi_i^2 a_i^2 \right\rangle + \left\langle \sum_{i\neq j} \phi_i\phi_j a_i a_j \right\rangle = (1-\xi)\sum_i a_i^2 + (1-\xi)^2 \sum_{i\neq j} a_i a_j,$$

and the first term can be neglected compared to the second one for a large number of asperities and for ξ which is not too close to 1, therefore

$$\langle \alpha_{\mathrm{HG}}(\xi)\rangle \approx \frac{\pi}{2}\frac{(\sum_i a_i)^2}{\sum_{i,i\neq j}\sum_j a_i a_j/d_{ij}}.$$

The main drawback of this model is that a link between local spots, the macroscopic force acting on the system and the involved displacements is missing. A way out was proposed by the same author in [Greenwood and Tripp, 1967], which will be considered in the next subsection.

2.5 Greenwood-Tripp model

To make a truly predictive model linking contact area and force in contact of rough spheres, Greenwood and Tripp constructed a model taking into account averaged deformations induced by the contact pressure due to asperity contact [Greenwood and Tripp, 1967]. This model, initially constructed for spherical contact, can be extended to arbitrary contact shape (its numerical implementation for the axisymmetric contact is provided in [Yastrebov, 2025b]).

The key idea of the model is that it solves the problem within a fixed-point iterative procedure: approaching between rough surfaces results in asperity-induced pressure, which should induce surface deflection, which in turn change the approaching between surfaces, an equilibrium state should exist. At every iteration i, it computes pressure distribution $p^i(x,y)$ from the separation field $z^i(x,y)$ using, for example, Greenwood-Williamson (GW) multi-asperity model [Greenwood and Williamson, 1966], then it computes induced displacement field $u^i(x,y)$ using integral convolution, it further recomputes the separation $z^{i+1}(x,y)$ and so on until the convergence. The pressure $p^i(x,y)$ induced by asperity contact based on GW statistical multi-asperity model for the separation $z_0^i(x,y)$ between two surfaces is given by the following equation

$$p^i(x,y) = \tfrac{4}{3}\eta E^* \beta^{1/2} \int_{z_0^i(x,y)}^{\infty} (z - z_0^i(x,y))^{3/2} P(z)\, dz, \tag{16}$$

where η is the asperity density, β their average geometrically mean curvature radius, and $P(z)$ is the probability density of asperity heights. The pressure-induced macroscopic normal deflection of the surface can be computed following Boussinesq approach: the total induced displacement (summing up both deforming surfaces) is given by

$$u_z^i(x,y) = \frac{1}{\pi E^*} \int_{\mathbb{R}^2} \frac{p^i(x',y')\,dx'dy'}{\sqrt{(x-x')^2+(y-y')^2}}. \tag{17}$$

Then the separation between the surfaces is updated $z_0^{i+1} = z_0^i + u^i$, new pressure p^{i+1} is recomputed (16), and the induced displacement u^{i+1} from (17) and so on until convergence. For an axisymmetric problem, a simpler form is available [Johnson, 1987, Eq. (3.96a)]:

$$u_z^i(r) = \frac{4}{\pi E^*} \int_0^\infty \frac{\rho}{\rho + r}\, p^i(\rho)\, K(k(r,\rho))\, d\rho \tag{18}$$

where r and ρ are the radial coordinates and the modulus k of the complete elliptic integral of the first kind $K(k)$ is given by:

$$k(r,\rho) = \frac{4\rho r}{(r+\rho)^2}, \quad K(k) = \int_0^{\pi/2} [1 - k\sin^2(t)]^{-1/2}\, dt. \tag{19}$$

At the converged separation $z^*(x,y)$, using the fact that the contact area of Hertz contact of j-th spot is $A_j = \pi\beta\delta_j$ where δ_j is the corresponding local approaching, we can obtain the statistical contact area fraction as

$$A^*(x,y) = \pi\eta\beta \int_{z^*(x,y)}^{\infty} (z - z^*(x,y))\, P(z)\, dz. \tag{20}$$

If one assumes that asperities follow a normal distribution with the standard deviation σ, we obtain a closed form:

$$A^*(x,y) = \pi\eta\beta \left[\frac{\sigma}{\sqrt{2\pi}} \exp\left(-\frac{z^{*2}(x,y)}{2\sigma^2} \right) - z^* \operatorname{erfc}\left(\frac{z^*(x,y)}{\sqrt{2}\sigma} \right) \right]. \tag{21}$$

Note that the whole model in the presented form can be readily used for an arbitrary indenter's shape, using either Eq. (16) for the general case or Eq. (17) for the axisymmetric one.

Using Eq. (21), we can demonstrate how the contact area decays far from the core contact region for a parabolic indenter of radius R^*. If we ignore the elastic deformation decaying nominally as $\sim 1/r$, the surface profile is given by $z^* \sim r^2/(2R^*) - \delta$, where δ is the initial separation at the tip. Then the contact area fraction for large r can be approximated by the following decay

$$A^* \approx \pi\eta\beta \left[\frac{\sigma}{\sqrt{2\pi}} \exp\left(\frac{-r^4}{8R^{*2}\sigma^2} \right) \exp\left(\frac{\delta(r^2 - \delta R^*)}{2R^*\sigma^2} \right) - \left(\frac{r^2}{2R^*} - \delta \right) \operatorname{erfc}\left(\frac{r^2 - 2\delta R^*}{2\sqrt{2}R^*\sigma} \right) \right], \tag{22}$$

which results in an extremely rapid (super-Gaussian) asymptotic decay $A^* \sim \exp(-r'^4/8)$ with the natural normalized parameter $r' = r/\sqrt{R^*\sigma}$ (see Fig. 4(d)).

Parameter	Symbol	Value	Units
Material Properties			
Young's modulus	E	2.1×10^{11}	Pa
Poisson's ratio	ν	0.3	-
Combined modulus (steel-on-steel)	E^*	$\approx 1.15 \times 10^{11}$	Pa
Resistivity (steel)	ρ^*	7.2×10^{-7}	Ωm
Roughness Parameters			
RMS roughness	σ	20	μm
Asperity density	η	2×10^8	m^{-2}
Asperity tip radius	β	30	μm
Indenter Geometry			
Indenter radius	R^*	10	mm
Loading Parameters			
Initial separation at $r = 0$	δ	$-40 = -2\sigma$	μm
Numerical Parameters			
Convergence tolerance	ε	10^{-3}	-
Relaxation parameter	ζ	0.3	-

Table 1: Greenwood-Trip test model parameters.

2.5.1 Greenwood-Trip model example

Let us consider indentation of an elastic half-space by an elastic parabolic indenter of radius R^*. The roughness parameter α introduced in [Greenwood et al., 1984] takes the following form

$$\alpha = \frac{\sigma R}{a^2},$$

where σ is the RMS of asperity distribution, R^* is the effective curvature and a is the contact radius for the associated Hertz problem ignoring surface roughness. This parameter determines whether the Hertz contact assumptions of smooth idealized surfaces provides accurate results, the case when $\alpha \ll 1$, or the surface roughness has to be carefully taken into account, the case when $\alpha \sim 1$. For the set of parameters provided in Table 1, the roughness parameter is $\alpha \approx 0.361$, thus placing this problem in the class of problems where the deviation from the Hertz theory is significant due to the surface roughness. The obtained pressure, contact area distribution, deformed configuration and the resulting surface displacement are shown in Fig. 4 and compared with the reference Hertz solution for the same load. Following [Greenwood and Tripp, 1967], we normalize the pressure by $\bar{p} = E^*\sqrt{\sigma R^*}$.

To simplify the convergence, we use a relaxation technique by weighting the obtained displacement increment at iteration $k+1$ with ζ as

$$u'_{k+1} = \zeta u_{k+1} + (1-\zeta)u_k,$$

Therefore, the change in displacement is given by $u'_{k+1} - u_k = \zeta(u_{k+1} - u_k)$, and for the convergence we will require that

$$\frac{\|u_{k+1} - u_k\|_\infty}{\|u_k\|_\infty} \leq \varepsilon \quad \Leftrightarrow \quad \frac{\|u'_{k+1} - u_k\|_\infty}{\|u_k\|_\infty} \leq \zeta\varepsilon.$$

The iterative algorithm converges in 12 iterations for $\zeta = 0.3$ and tolerance $\varepsilon = 10^{-3}$. The Python implementation is available at [Yastrebov, 2025b].

2.5.2 From continuous to discrete Greenwood-Tripp model

At the convergence of the iterative algorithm, we obtain continuous and smooth fields of pressure $p^*(r)$, contact area fraction $A^*(r)$ and displacement $u(r)$, which have to be interpreted in a statistical sense as ensemble averages (see [Yastrebov, 2019]). Assuming a relatively high asperity density η we can split the contact area into a square grid $\Delta x \times \Delta x$ with $\Delta x = 1/\sqrt{\eta}$, then every grid contains in average only one asperity. An evolution of such contact area representation is visualized in Fig. 5 for different approaches $\delta/\sigma \in \{2.00,\ 0.00,\ -1.75,\ -3.00\}$. Along with the true contact area, we plot circles corresponding to Hertzian contact radius and the Holm-Greenwood interaction radius (13). Note that the latter is bigger and considerably bigger for lighter contacts, but at higher loads the Holm-Greenwood interaction radius converges to the Hertzian one. Note also that the contact spots at asperities are almost invisible to the naked eye for light loads but become pronounced for higher loads.

With this model interpretation, one can draw the contact picture which would bring us to Greenwood's model (Section 2.4) and analyze the effect of the insulating oxide for this contact distribution. This connection represents the core contribution of this paper.

2.6 Oxide modelling

Oxides can grow differently on surfaces depending on the environment, stress state, crystal orientation, surface defects, temperature, and surface curvature. Here, we adopt a particular case of oxide morphology when it forms: (1) completely separate islands, consistent with the Volmer-Weber growth model [Venables et al., 1984, Herman et al., 2013], or (2) thicker insulating islands on a substrate of a very thin, still-conductive oxide layer. The first situation (1) typically occurs when metal oxides are formed on noble metal substrates, such as MgO or FeO on Ag or Pt [Freund and Pacchioni, 2008].

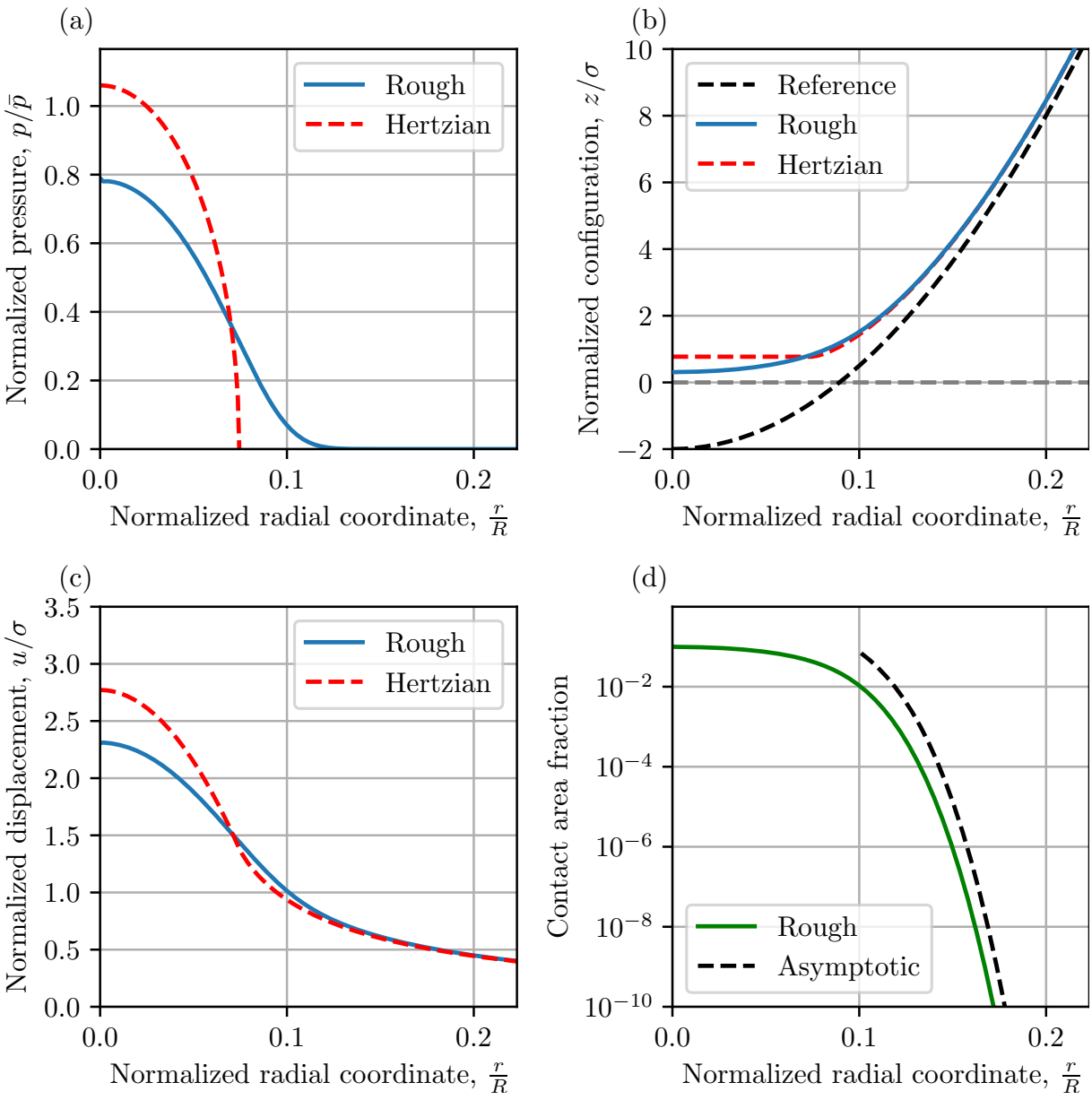

Figure 4: Illustration of Greenwood-Tripp model: (a) – pressure distribution and the corresponding Hertzian pressure; (b) – initial penetration (dashed line) and the resulting indenter's configuration compared with the Hertzian configuration; (c) – vertical displacement compared with the Hertzian displacement; (d) contact area fraction for Greenwood-Tripp model in semi-log scale and the asymptotic decay (22). Model parameters used to obtain these results are summarized in Table 1.

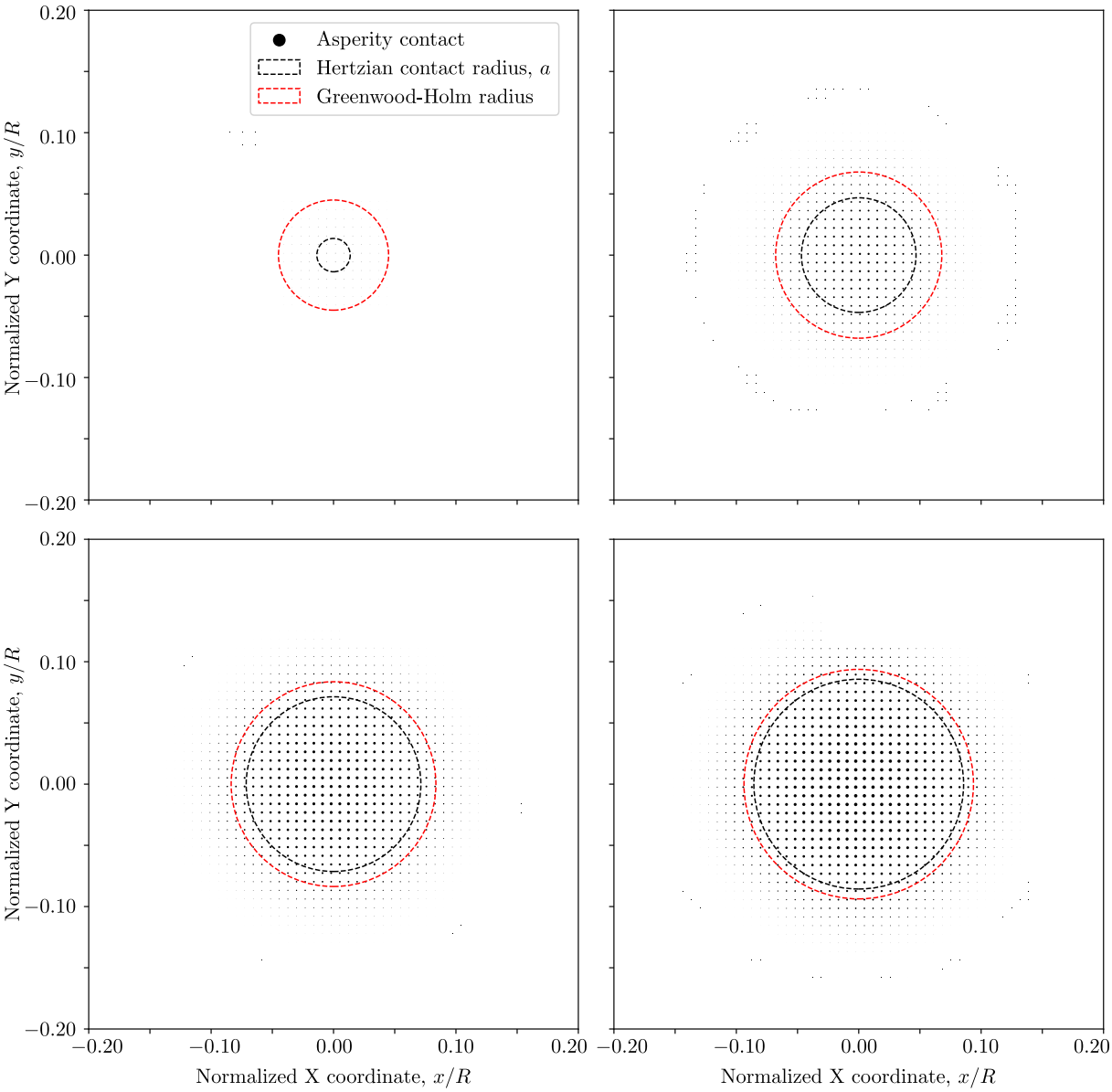

Figure 5: Evolution of the contact area at asperities computed using Greenwood-Tripp model for $\delta/\sigma \in \{2.00,\ 0.00,\ -1.75,\ -3.00\}$ (shown from left to right). The corresponding Hertz radius and the Holm-Greenwood radius (13) are also shown.

In these cases, the high interfacial energy promotes the formation of localized hemispherical islands rather than a wetting film. The second situation (2) is characteristic of chromia (Cr_2O_3) growth, where a precursor ultrathin layer may form before the nucleation of bulk-like insulating islands [Maurice et al., 1994]. Similar heterogeneous morphology is observed in the high-temperature oxidation of Cu to form Cu_2O [Zhou and Yang, 2003, Gattinoni and Michaelides, 2015]. Another possibility is (3) the spalling, cracking, channeling and debonding of oxide films [Evans, 1994, Evans and Hutchinson, 1995, Li et al., 2022], which can produce partially exposed or non-conductive structures that may also be modeled within our framework. From an electric perspective, these insulating islands act as obstacles to surface current, and the electric resistance is thus governed by their morphology and percolation rather than the overall film thickness, making island-based models applicable to this class of oxides.

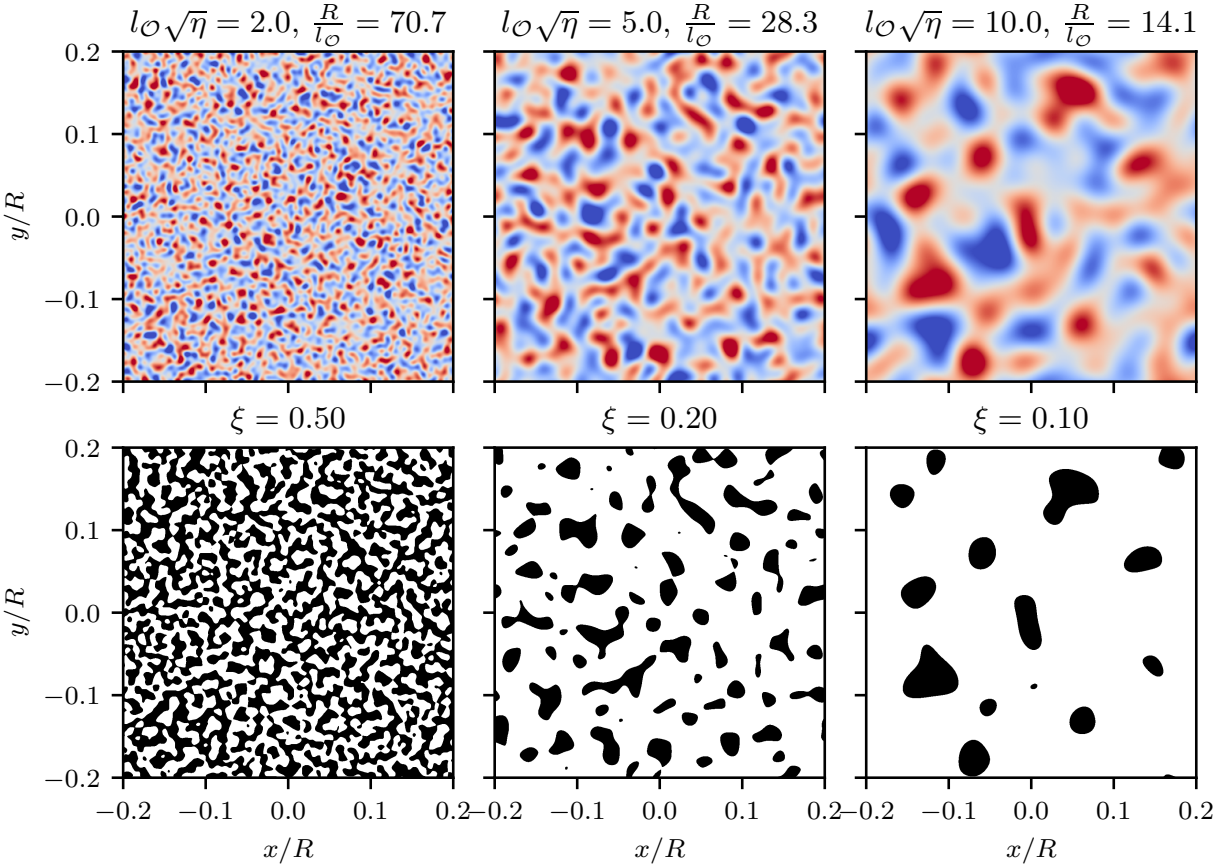

Figure 6: *Upper panel:* random fields with different lower frequency cutoff defining the correlation length $\lambda = l_O\sqrt{\eta} = \{2,5,10\}$, note that $R\sqrt{\eta} \approx 141.42$. *Lower panel:* resulting thresholded oxides for $\xi = \{50,20,10\}$ %.

To model this type of oxides, we first generate a Gaussian random field $\psi(x,y) \sim \mathcal{N}(0,1)$ with a self-affine isotropic spectrum $\Phi(k) \sim k^{-2(1+H)}$, where $H \in (0,1)$ is the Hurst exponent, the absolute value of the wavevector $k = \sqrt{k_x^2 + k_y^2}$ is bounded within an interval $k_l \le k \le k_s$. Wavenumbers k_l and k_s correspond to low and high frequency cutoffs. So, to leading order the correlation length is determined by π/k_l. The oxide film location is defined by an indicator Heaviside function:

$$O(x,y) = H(\psi(x,y) - \psi_0) = \begin{cases} 1, & \text{if } \psi(x,y) - \psi_0 \ge 0 \\ 0, & \text{else.} \end{cases} \tag{23}$$

As a consequence, the characteristic lateral correlation length of the oxide islands is inherited from the

underlying field and can be estimated as

$$l_O = \frac{\pi}{k_l}$$

To obtain the threshold ψ_0 for a given oxide fraction ξ, we can use the following equation

$$\psi_0 = \sqrt{2}\,\mathrm{erfc}^{-1}(2\xi),$$

which could be further refined using the bisection algorithm. In Fig. 6, several realizations of oxide films and underlying random fields are shown.

To make a link between relevant length scales of the surface roughness and oxide islands, we introduce the dimensionless correlation length λ:

$$\lambda = l_O\sqrt{\eta} = \frac{l_O}{d},$$

where η is the asperity density and $d = 1/\sqrt{\eta}$ is the average spacing between asperities. Then, small values of $\lambda \ll 1$ would correspond to oxide islands considerably smaller than the spacing between asperities, whereas larger values $\lambda \gg 1$ imply that every island contains multiple asperities.

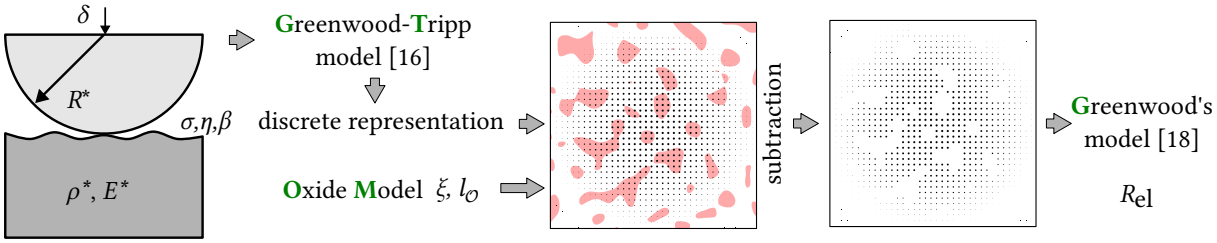

Figure 7: An illustration of the Greenwood^2-Tripp Oxidized Model (G^{2}TOM) workflow for evaluating the electric contact resistance R_{el}. The model inputs include the approach δ, effective material parameters: E^* for elastic and ρ^* for electric, and roughness parameters σ, η, and β. The mechanical contact problem is first solved using the Greenwood-Tripp model [Greenwood and Tripp, 1967], and the resulting discrete spatial distribution of contact spots is mapped onto the xy-plane. On the top, a generated random map of insulating oxide film, characterized by parameters ξ and l_O, is superimposed. Contact spots covered by oxide islands are removed from the conductive set. Finally, the constriction resistance problem is solved for the remaining active contact spots using Greenwood's model [Greenwood, 1966] to determine R_{el}. Multiple oxide maps are generated to perform a statistical analysis of the contact resistance.

2.7 Greenwood^2-Tripp Oxidized Model (G^{2}TOM)

To study the effect of oxides and roughness on the electric contact resistance, we assemble the three ingredients: (1) the discretized version of the Greenwood-Tripp model, (2) the oxide film model and (3) Greenwood's conductivity model; these three models give an abbreviated name G^{2}TOM. The workflow is illustrated in Fig. 7. For the contact area obtained by the Greenwood-Tripp and discretized in regularly spaced cells with the size $\Delta x = 1/\sqrt{\eta}$, we can check for every contact spot whether it is covered by oxide film or not. If the i-th contact spot's center is covered by oxide $\{x_i, y_i\} \in O$, then we will assume that this spot does not take part in conductivity. Otherwise, the asperity contact area is assumed to perfectly conduct electricity. As soon as this labeling and mapping is done, we will use Greenwood's model (11) on conductive spots to evaluate electric contact resistance.

3 Results

For every combination of oxide correlation length l_O and its fractions ξ, we constructed 500 random oxide fields. Following the G^{2}TOM receipt, these random fields are superposed with the discrete Greenwood-

Tripp model results and the electric resistance is evaluated using Greenwood's model. The parametric study follows the parameters listed in Table 2 resulting in 54 000 oxide configurations. These maps are superposed with Greenwood-Trip discretized results for 20 load steps, thus resulting in 1 080 000 simulations which took 68 minutes on 20 cores with an optimized python code shared along with data in [Yastrebov, 2025a].

Parameter	**Interval**	**Number of values**
Random Gaussian field	-	500
Oxide fraction, ξ	$(0.1, 0.9)$	9
Normalized oxide correlation length, $\lambda = l_O\sqrt{\eta}$	$(1, 23)$	12
Normalized approach, δ/σ	$(2, -3)$	20

Table 2: List of parameters for the parametric study resulting in 54 000 oxide configurations and 1 080 000 simulations. All other parameters are listed in Table 1.

The simulation results are shown in Fig. 8 for different values of insulating oxide fractions ξ and different values of the normalized oxide correlation length $\lambda = l_O\sqrt{\eta}$. The results are systematically compared with the clean surface resistance. The average value computed over 500 realizations is complemented by 16 %-84 % percentiles shown with a shaded area. All the data for the established contact electric resistance R_{el} can be fitted by a power law

$$R_{\mathrm{el}} = \alpha_0 \left(\frac{F}{F_0}\right)^{-\gamma}, \tag{24}$$

with $F_0 = 1\,\mathrm{N}$ and α_0 being a dimensional parameter. We can notice that the decay exponent is $\gamma \approx 0.23$ for the clean surface; it systematically increases with the oxide fraction ξ. To recover dimensional results, the resistivity of steel is used. Note that increase in the oxide correlation length l_O expectedly results in an increase in the dispersion of conductivity, which also represents an important characteristic for the rough oxidized electric contact.

Using the normalization proposed by Barber in [Barber, 2003], we obtain the following forms for the contact electric resistance R'_{el} and conductance κ':

$$R'_{\mathrm{el}} = \alpha F'^{-\gamma}, \qquad \kappa' = \frac{1}{\alpha} F'^{\gamma}, \tag{25}$$

where

$$R'_{\mathrm{el}} = \frac{R_{\mathrm{el}}\sqrt{R^*\sigma}}{2\rho^*}, \qquad F' = \frac{2F}{E^*\sqrt{R^*\sigma^3}}.$$

Following this equation, we can readily transform factor α_0 to α as

$$\alpha = \frac{\alpha_0}{2\rho^*}\left(\frac{2F_0}{E^*}\right)^{\gamma} R^{*\frac{1-\gamma}{2}} \sigma^{\frac{1-3\gamma}{2}}.$$

The normalized electric conductance evolution with the normalized force is plotted in Fig. 9 for different oxide fractions and different correlation lengths.

3.1 Fitting procedure

For every combination of ξ and λ, for the mean behavior we fitted the power law constants: the factor α and the exponent γ (see Fig. 10). We approximated the tabulated dependences $\alpha(\xi,\lambda)$ and $\gamma(\xi,\lambda)$ on the (λ,ξ) grid using a low-rank separable surrogate. For each parameter, the data matrix $M_{ij} = M(\lambda_i, \xi_j)$ was decomposed by singular value decomposition and truncated to rank r, yielding

$$M(\lambda,\xi) \approx \sum_{k=1}^{r} u_k(\lambda)\, v_k(\xi). \tag{26}$$

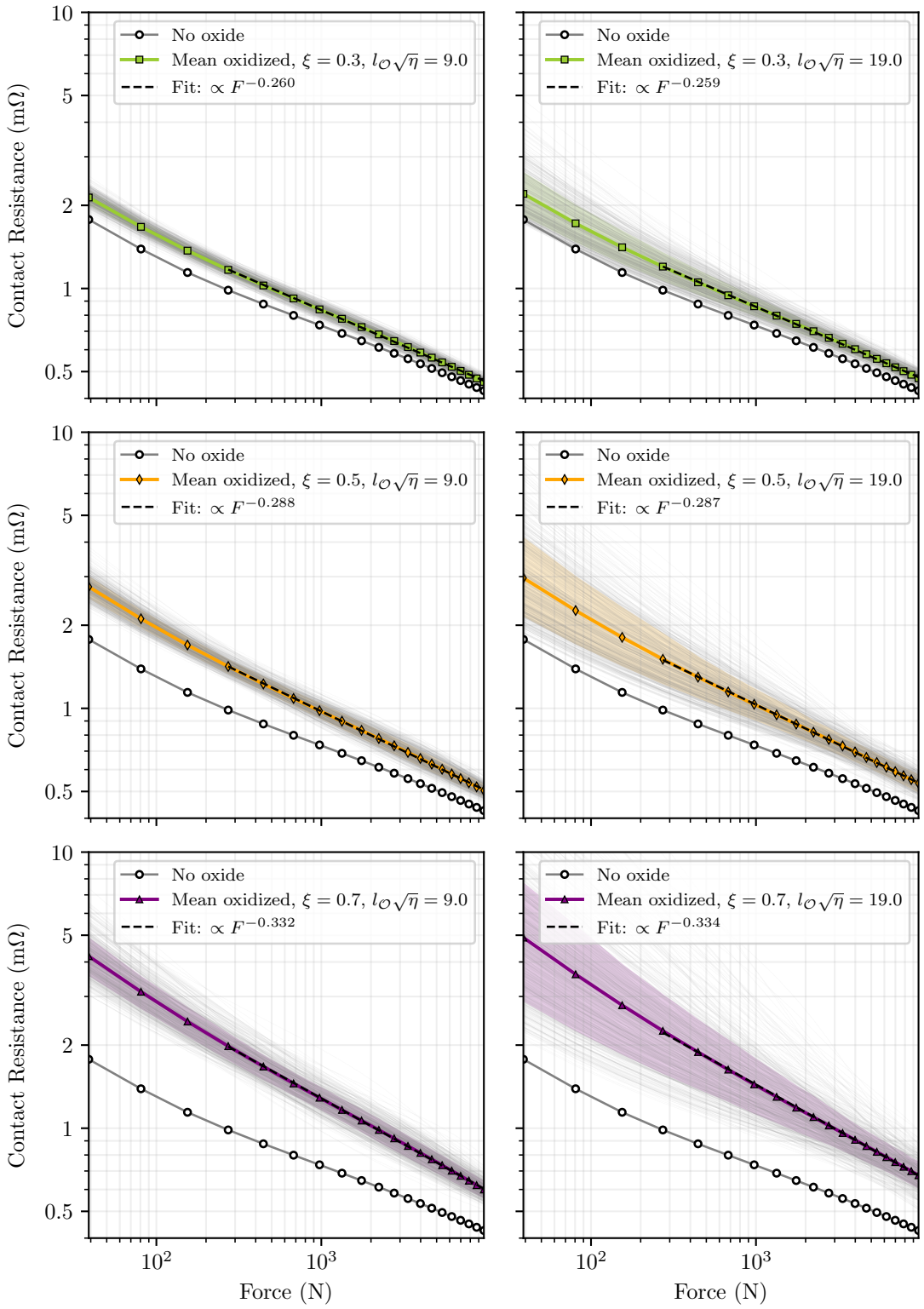

Figure 8: Electric contact resistance for a steel spherical indenter of radius $R = 10mm$ on a flat steel surface in presence of insulating oxide films of different surface fraction $\xi = \{0.3,\ 0.5,\ 0.7\}$ and different spatial correlation $l_O\sqrt{\eta} = \{9,\ 19\}$. Shaded area corresponds to 16-84 percentiles boundary and the markers correspond to the geometric mean. Individual results are shown as semi-transparent gray lines. The data are fit by a power law (25).

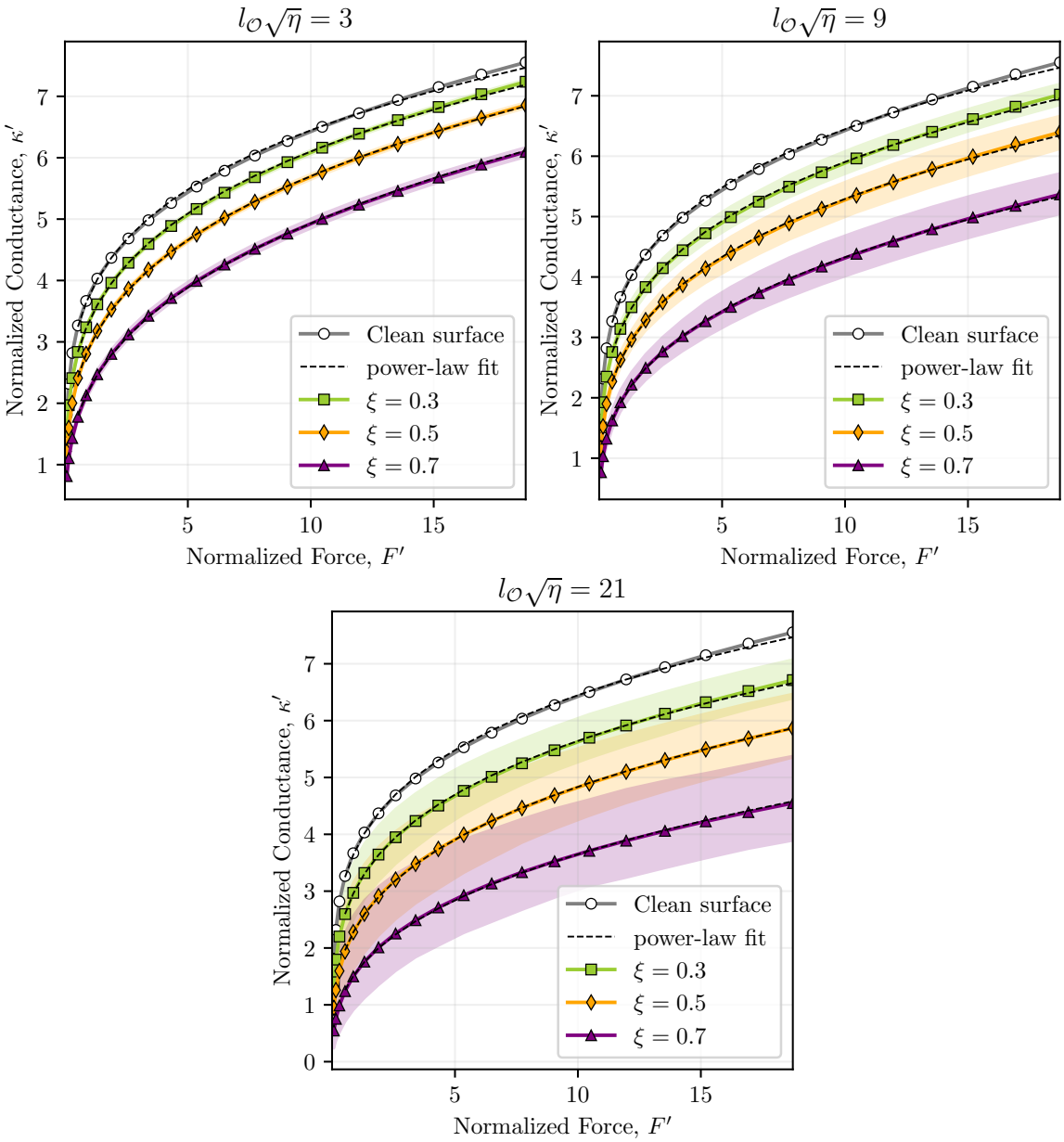

Figure 9: Normalized electric contact conductance for a steel spherical indenter of radius $R = 10\,\mathrm{mm}$ on a flat steel surface in presence of insulating oxide films of different surface fraction ξ and different spatial correlation $l_{\mathcal{O}}\sqrt{\eta}$. Shaded area corresponds to 16-84 percentiles boundary and the markers correspond to the geometric mean; the data are fit by a power law (25).

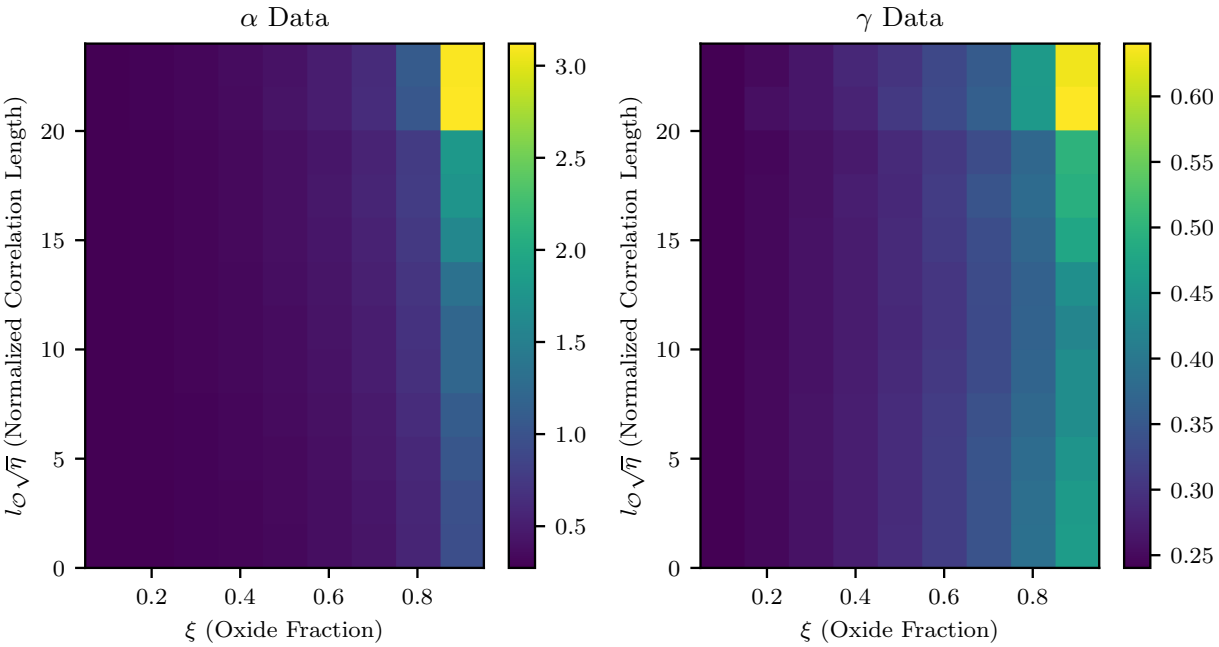

Figure 10: Least mean-squared fitted factor α and exponent γ evaluated over parameters given in Table 2, which were in turn approximated by reduced SVD (26) with coefficients presented in Table 4.

To obtain smooth continuous functions, we fitted the one-dimensional mode shapes in transformed coordinates that better resolve the sharp variation at large ξ, using $w = \log\lambda$ and $z = -\log(1-\xi)$, and approximated $u_k(w)$ and $v_k(z)$ by low-order polynomials. This yields a compact analytic representation with $r[(p_u+1)+(p_v+1)]$ coefficients while accurately reproducing the original grid values, including the strong corner nonlinearity as $z\xi \to 1$ and at high values of λ. We used SVD up to rank $r = 2$, and an optimized set of polynomial orders was selected. For $\alpha(z(\xi), w(\lambda))$ we used order 2 for z and order 3 for w, whereas for $\gamma(z(\xi), w(\lambda))$ we used order 1 for z and order 2 for w, thus givien in total 14 parameters to fit α and 10 to fit γ, these parameters are shown in Table 4. All the data are available in [Yastrebov, 2025a].

Finally, we obtain the following phenomenological model to estimate the electric contact resistance of rough contact under parabolic indenter:

$$\boxed{R_{\mathrm{el}} = \alpha(\xi, l_O\sqrt{\eta})\frac{2\rho^*}{\sqrt{R^*\sigma}}\left(\frac{2F}{E^*\sqrt{R^*\sigma^3}}\right)^{-\gamma(\xi, l_O\sqrt{\eta})}} \tag{27}$$

where the factor $\alpha(\xi, l_O\sqrt{\eta})$ and the exponent $\gamma(\xi, l_O\sqrt{\eta})$ depend on the oxide fraction ξ and the oxide correlation length normalized by the average distance between asperities defined by the asperity density $l_O\sqrt{\eta}$.

3.2 Roughness parameters

The Greenwood-Tripp model requires the asperity density parameter; in practical case it can be obtained for a rough surface through the following relation

$$\eta = \frac{\sqrt{3}}{18\pi}\frac{m_4}{m_2},$$

where m_2 and m_4 are spectral moments of the isotropic surface roughness [Nayak, 1971]. Another roughness parameter is the standard deviation of asperities σ which is, in general smaller, than the surface roughness' standard deviation. The contrast is the highest for low values of Nayak's parameter, but the

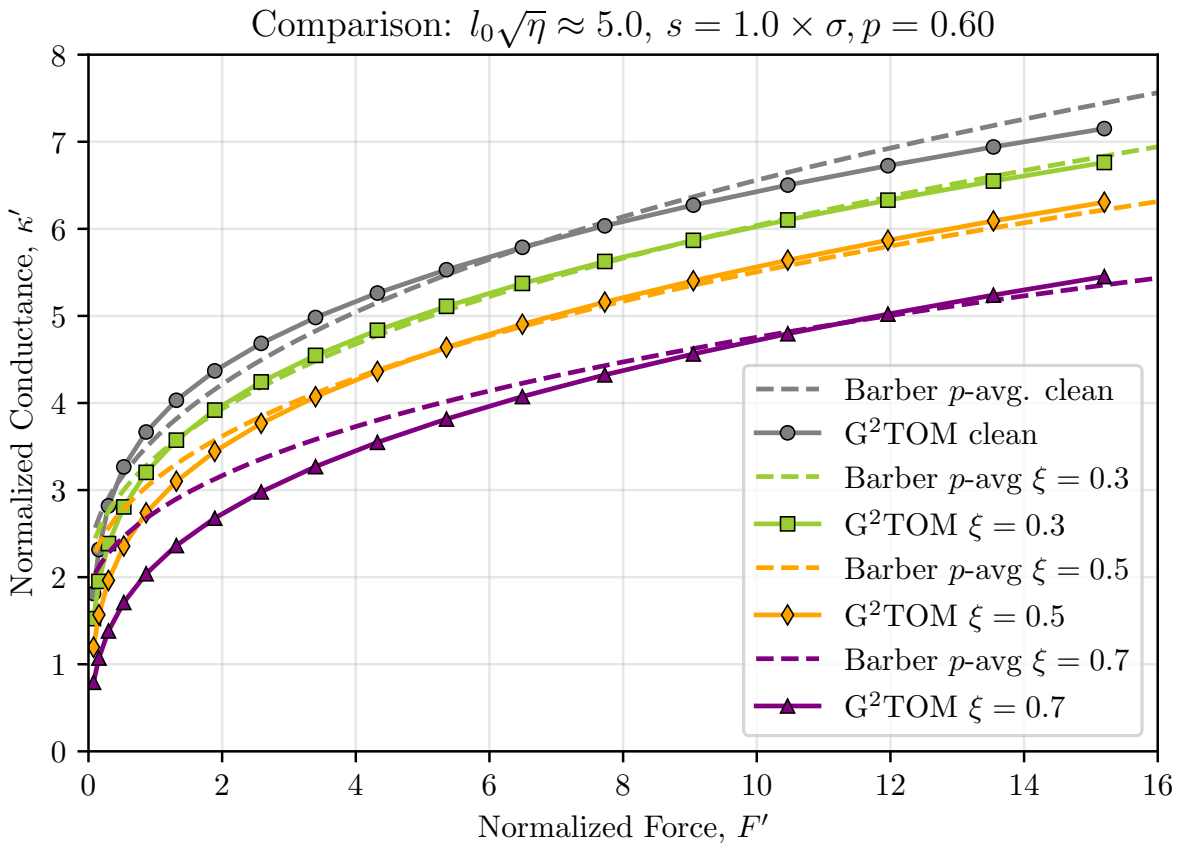

Figure 11: The G^{2}TOM model normalized with $s = \sigma$ is compared with the modified Barber's model using $\langle \kappa' \rangle_{p=0.6}$ average.

two parameters coincide for Nayak's parameter tending to infinity [Nayak, 1971, Yastrebov et al., 2017]. The last roughness parameter is the average asperity curvature radius. Following [Yastrebov, 2019, Greenwood, 2006], it can be estimated as

$$\beta = \frac{0.737}{\sqrt{m_4}}.$$

We must, however, admit that this mean curvature was omitted in the current analysis, its value defined in Table 1 was used throughout the study. Along with oxide density, β is one of central parameters which enters in pressure distribution as $\eta\sqrt{\beta}$ and the contact area distribution as $\eta\beta$ and it also defines the contact spot radii as $\sqrt{\eta\beta}$.

3.3 G^{2}TOM and Barber's bounds

Finally, we compare our model to the modified Barber's model accounting for oxides (10) by taking the p-average conductivity with $p = 0.6$ and $s = \sigma$ which appear to fit relatively well our results. The results are shown in Fig. 11. A relatively good agreement is obtained for the considered interval. However, it has to be remarked that the p-average with $p = 0.6$ represents a very arbitrary averaging as well as the choice of $s = \sigma$ for the normalization. Nevertheless, by this comparison we aim to highlight that both models predict relatively well the average behavior due to the presence of oxides and that the results of G^{2}TOM lie within the adjusted-for-oxide Barber's bounds.

4 Discussion and Conclusion

This paper develops a model for electric contact resistance taking into account surface roughness and the presence of isolated islands of insulating oxide films in the contact interface. The presence of these films does not allow to reduce the conductivity study to the study of the normal contact stiffness following the equivalence shown in [Barber, 2003], but requires a deeper analysis.

The model that we have constructed relies on two classical models: on the Greenwood-Tripp (GT) model for contact of rough spheres [Greenwood and Tripp, 1967] and on Greenwood's model for the constriction resistance [Greenwood, 1966]. It is worth noting that the GT model, originally constructed for an axisymmetric case, can be successfully used for an arbitrary indenter's shape. In essence, our model solves the rough elastic contact using the GT model, the contact area is then discretized in individual contact spots. On the top of this contacting asperities featuring different contact area defined by the GT model, we superpose a random oxide field, generated as a thresholded Gaussian random field with controlled correlation length l_O. Solving now the conductivity problem using Greenwood's model [Greenwood, 1966] and ignoring contact zones screened by oxide films, we obtain the resulting conductance. The model is abbreviated as G^{2}TOM for *Greenwood^2-Tripp Oxide conductance Model*.

A parametric analysis demonstrates that the increase in oxide fraction ξ logically results in a decrease of conductance, whereas the increase in the oxide correlation length results in the increase of the dispersion of results. When the correlation length of oxide islands is comparable with the average distance between contacting asperities $l_O\sqrt{\eta} < 5$ (with η being the asperity density) the dispersion of results is minimal; however for $l_O\sqrt{\eta} > 10$ a strong dispersion is observed. The average conductance change is well described by a power law of the contact force with the factor and the exponent depending on the oxide fraction and weakly depending on the correlation length. However, for high oxide fractions, the correlation length starts to strongly influence the conductance. The obtained results, however, do not integrate the dependence on the mean asperity curvature β, which requires an additional study.

To capture this non-trivial dependence of parameters on the oxide fraction and its correlation length, we constructed a truncated SVD-polynomial fitting model with a special mapping of these parameters. The constructed phenomenological model can be easily used with the key parameters extracted from surface roughness spectrum.

This paper also suggests an adjustment to Barber's bounds [Barber, 2003] on the electric resistance of rough spherical contact to take into account the effect of oxides in the contact interface using geometrical considerations and the Love's solution for a conducting annulus. Using Barber's normalization, we show that for the key parameter of his model[2] set to $s = \sigma$, and for the specially chosen p-average between the adjusted bounds with $p = 0.6$, we obtain a good agreement between the extended Barber's model and the G^{2}TOM.

It is important to remark that the model constructed here relies on the statistical roughness description and the ensemble-averaged results and thus, it cannot predict from the mechanical point of view the situation where a single or only a few asperities come in contact as discussed in [Ciavarella et al., 2008, Yastrebov, 2019], which would result in change of regime between light and moderate loads. However, we need to bear in mind that the electric model deals with the discretized Greenwood-Tripp results, i.e. with individual and deterministic contact spots. In practice, at very light loads, a single-asperity contact must produce and the approach-force-resistance will be determined exclusively by this contact.

Another remark is that the effect of oxide cracking and spallation – which is so common in electric conductance and probably, presents the main mechanism to ensure electric conductivity for numerous oxidized contacts – was not considered in this study.

Our model can be extended to take into account a reduced conductivity of the oxide film instead of assuming it fully insulating. This change can be integrated in Greenwood's constriction model.

To make a next step in this study, a more rigorous analysis is needed. Hence, we plan to carry out accurate contact simulations of rough surfaces as in [Yastrebov et al., 2017] accompanied by conductivity

[2]Parameter s in Barber's model characterizes the difference between the height of the first contact and the deepest contact depth.

simulations as in [Beguin and Yastrebov, 2025]. Such simulations will permit also to tune better the simplified model presented here. However, it would be computationally much more expensive to carry out as many simulations as we have been carried out here with the simplified model - more than one million.

Acknowledgement

The author is grateful to Paul Beguin, Samuel Forest and Cristian Ovalle-Rodas for thoughtful discussions.

References

[Barber, 2003] Barber, J. (2003). Bounds on the electrical resistance between contacting elastic rough bodies. *Proceedings of the royal society of London. Series A: mathematical, physical and engineering sciences*, 459(2029):53–66.

[Barber, 2013] Barber, J. (2013). Incremental stiffness and electrical contact conductance in the contact of rough finite bodies. *Physical Review E*, 87(1):013203.

[Beguin and Yastrebov, 2025] Beguin, P. and Yastrebov, V. A. (2025). Electrical and thermal conductivity of complex-shaped contact spots. *Comptes Rendus. Mécanique*, 353(G1):195–234.

[Ciavarella et al., 2008] Ciavarella, M., Dibello, S., and Demelio, G. (2008). Conductance of rough random profiles. *International Journal of Solids and Structures*, 45(3-4):879–893.

[Evans and Hutchinson, 1995] Evans, A. and Hutchinson, J. (1995). The thermomechanical integrity of thin films and multilayers. *Acta Metallurgica et Materialia*, 43(7):2507–2530.

[Evans, 1994] Evans, H. (1994). Modelling oxide spallation. *Materials at high temperatures*, 12(2-3):219–227.

[Freund and Pacchioni, 2008] Freund, H.-J. and Pacchioni, G. (2008). Oxide ultra-thin films on metals: new materials for the design of supported metal catalysts. *Chemical Society Reviews*, 37(10):2224–2242.

[Gattinoni and Michaelides, 2015] Gattinoni, C. and Michaelides, A. (2015). Atomistic details of oxide surfaces and surface oxidation: the example of copper and its oxides. *Surface Science Reports*, 70(3):424–447.

[Greenwood, 2006] Greenwood, J. (2006). A simplified elliptic model of rough surface contact. *Wear*, 261(2):191–200.

[Greenwood et al., 1984] Greenwood, J., Johnson, K., and Matsubara, E. (1984). A surface roughness parameter in Hertz contact. *Wear*, 100(1-3):47–57.

[Greenwood and Williamson, 1966] Greenwood, J. and Williamson, J. (1966). Contact of nominally flat surfaces. *Proceedings of the Royal Society of London. Series A. Mathematical and Physical Sciences*, 295(1442):300–319.

[Greenwood, 1966] Greenwood, J. A. (1966). Constriction resistance and the real area of contact. *British Journal of Applied Physics*, 17(12):1621.

[Greenwood and Tripp, 1967] Greenwood, J. A. and Tripp, J. H. (1967). The elastic contact of rough spheres. *Journal of Applied Mechanics*, 34(1):153–159.

[Helmholtz, 1860] Helmholtz, H. (1860). Theorie der luftschwingungen in röhren mit offenen enden. *Journal für die reine und angewandte Mathematik*, 57:1–72.

[Herman et al., 2013] Herman, M. A., Richter, W., and Sitter, H. (2013). *Epitaxy: physical principles and technical implementation*. Springer, Berlin–Heidelberg.

[Holm, 1967] Holm, R. (1967). *Electric Contacts*. Springer, Berlin.

[Johnson, 1987] Johnson, K. L. (1987). *Contact mechanics*. Cambridge university press, Cambridge.

[Lee et al., 2011] Lee, K. Y., Jeong, D. K., and Kim, J. H. (2011). Simulational study of electrical contact degradation under fretting corrosion. *Tribology international*, 44(12):1651–1658.

[Li et al., 2022] Li, M., Wang, P., Yang, Y.-Q., Yang, Y.-Z., Pei, H.-Q., Wen, Z.-X., and Yue, Z.-F. (2022). Oxidation behavior of a nickel-based single crystal superalloy at 1100° C under different oxygen concentration. *Journal of Materials Science*, 57(5):3822–3841.

[Liu et al., 2015] Liu, H., Leray, D., Colin, S., and Pons, P. (2015). Finite element modeling of nickel oxide film for Au-Ni contact of MEMS switches. In *2015 IEEE 61st Holm Conference on Electrical Contacts (Holm)*, pages 266–272. IEEE.

[Love, 1976] Love, E. R. (1976). Inequalities for the capacity of an electrified conducting annular disc. *Proceedings of the Royal Society of Edinburgh Section A: Mathematics*, 74:257–270.

[Maurice et al., 1994] Maurice, V., Yang, W., and Marcus, P. (1994). XPS and STM investigation of the passive film formed on Cr (110) single-crystal surfaces. *Journal of The Electrochemical Society*, 141(11):3016.

[Müser et al., 2017] Müser, M. H., Dapp, W. B., Bugnicourt, R., Sainsot, P., Lesaffre, N., Lubrecht, T. A., Persson, B. N., Harris, K., Bennett, A., Schulze, K., et al. (2017). Meeting the contact-mechanics challenge. *Tribology Letters*, 65(4):118.

[Nayak, 1971] Nayak, P. R. (1971). Random process model of rough surfaces. *Journal of tribology*.

[Pastewka et al., 2025] Pastewka, L., Vakis, A. I., Aghababaei, R., Almqvist, A., Carbone, G., Chandross, M., Dini, D., Eder, S. J., Ehrich, H. J., Ewen, J. P., et al. (2025). Modeling in tribology: Recent advances, applications, and open questions. *Tribology International*, page 111326.

[Persson, 2022] Persson, B. N. (2022). On the electric contact resistance. *Tribology Letters*, 70(3):88.

[Sevostianov, 2010] Sevostianov, I. (2010). Incremental elastic compliance and electric resistance of a cylinder with partial loss in the cross-sectional area. *International Journal of Engineering Science*, 48(6):582–591.

[Strutt, 1871] Strutt, J. W. (1871). On the theory of resonance. *Philosophical Transactions of the Royal Society of London*, (161):77–118.

[Timsit, 2014] Timsit, R. S. (2014). Electrical contact resistance: Fundamental principles. In Slade, P. G., editor, *Electrical Contacts: Principles and Application*, pages 3–104. CRC Press, Boca Raton, FL, 2nd edition.

[Venables et al., 1984] Venables, J., Spiller, G., and Hanbucken, M. (1984). Nucleation and growth of thin films. *Reports on progress in physics*, 47(4):399.

[Yastrebov, 2019] Yastrebov, V. A. (2019). The elastic contact of rough spheres investigated using a deterministic multi-asperity model. *Journal of Multiscale Modelling*, 10(01):1841002.

[Yastrebov, 2025a] Yastrebov, V. A. (2025a). Accompanying scripts and dataset for the paper "Electrical conductance of oxidized rough sphere contacts: A Greenwood-Tripp-based model". available at Zenodo https://doi.org/10.5281/zenodo.18421705.

[Yastrebov, 2025b] Yastrebov, V. A. (2025b). Greenwood-Trip rough contact model. available at https://github.com/vyastreb/Greenwood-Tripp-Model.

[Yastrebov et al., 2017] Yastrebov, V. A., Anciaux, G., and Molinari, J.-F. (2017). The role of the roughness spectral breadth in elastic contact of rough surfaces. *Journal of the Mechanics and Physics of Solids*, 107:469–493.

[Zhou and Yang, 2003] Zhou, G. and Yang, J. C. (2003). Temperature effect on the Cu2O oxide morphology created by oxidation of Cu (0 0 1) as investigated by in situ UHV TEM. *Applied Surface Science*, 210(3-4):165–170.

Appendix A

Parameter α

ξ	$l_O\sqrt{\eta}$ 1	9	15	23
0.10	**0.274**	**0.276**	**0.277**	**0.279**
	0.264	0.272	0.278	0.247
	3.5%	1.3%	0.3%	11.6%
0.20	**0.284**	**0.290**	**0.294**	**0.299**
	0.279	0.289	0.302	0.302
	1.8%	0.3%	2.7%	1.2%
0.30	**0.297**	**0.308**	**0.315**	**0.326**
	0.296	0.308	0.325	0.346
	0.5%	0.1%	3.3%	6.0%
0.40	**0.315**	**0.332**	**0.341**	**0.368**
	0.317	0.331	0.351	0.381
	0.8%	0.5%	3.1%	3.5%
0.50	**0.340**	**0.366**	**0.385**	**0.415**
	0.346	0.361	0.383	0.415
	1.8%	1.6%	0.6%	0.1%
0.60	**0.377**	**0.415**	**0.446**	**0.498**
	0.389	0.405	0.432	0.472
	3.1%	2.2%	3.3%	5.1%
0.70	**0.439**	**0.496**	**0.541**	**0.621**
	0.460	0.482	0.524	0.623
	4.8%	2.9%	3.1%	0.3%
0.80	**0.565**	**0.669**	**0.752**	**1.087**
	0.602	0.642	0.748	1.115
	6.4%	4.1%	0.5%	2.6%
0.90	**0.960**	**1.210**	**1.595**	**3.100**
	1.000	1.120	1.535	3.251
	4.2%	7.4%	3.8%	4.9%

Parameter γ

ξ	$l_O\sqrt{\eta}$ 1	9	15	23
0.10	**0.241**	**0.241**	**0.240**	**0.241**
	0.240	0.241	0.242	0.244
	0.3%	0.2%	0.5%	1.2%
0.20	**0.249**	**0.250**	**0.249**	**0.251**
	0.250	0.250	0.250	0.251
	0.2%	0.1%	0.4%	0.1%
0.30	**0.260**	**0.260**	**0.259**	**0.265**
	0.261	0.261	0.261	0.260
	0.2%	0.3%	0.5%	1.9%
0.40	**0.273**	**0.272**	**0.270**	**0.284**
	0.274	0.274	0.273	0.273
	0.1%	0.5%	1.2%	3.9%
0.50	**0.291**	**0.288**	**0.288**	**0.301**
	0.289	0.289	0.290	0.292
	0.6%	0.5%	0.7%	3.0%
0.60	**0.313**	**0.307**	**0.309**	**0.326**
	0.307	0.309	0.312	0.319
	1.8%	0.7%	1.1%	2.2%
0.70	**0.342**	**0.332**	**0.334**	**0.356**
	0.331	0.336	0.344	0.362
	3.3%	1.1%	2.9%	1.8%
0.80	**0.388**	**0.369**	**0.373**	**0.458**
	0.364	0.375	0.395	0.436
	6.0%	1.6%	5.9%	4.6%
0.90	**0.462**	**0.436**	**0.477**	**0.631**
	0.421	0.448	0.498	0.603
	8.9%	2.7%	4.3%	4.5%

Table 3: Power-law fitted parameters α and γ for different oxide fractions ξ a selection of the normalized correlation length $l_O\sqrt{\eta}$; in every cell the number in bold is the fitted value, the second value is an approximation due to truncated SVD polynomial fit (26) and the percentage represents the relative error (below 5% colored in green, above - in red).

Fit for α			
Mode k	Function	Power p	Coefficient c_p
1	$U_k(w)$	w^2	-1.96×10^{-6}
		w^1	-4.37×10^{-4}
		w^0	-5.29×10^{-1}
	$V_k(z)$	z^3	-2.56×10^{-1}
		z^2	4.02×10^{-1}
		z^1	-4.15×10^{-1}
		z^0	-2.83×10^{-1}
2	$U_k(w)$	w^2	3.14×10^{-6}
		w^1	3.69×10^{-5}
		w^0	-3.12×10^{-1}
	$V_k(z)$	z^3	3.01×10^{-1}
		z^2	-6.59×10^{-1}
		z^1	3.12×10^{-1}
		z^0	-3.25×10^{-1}

Fit for γ			
Mode k	Function	Power p	Coefficient c_p
1	$U_k(w)$	w^1	-1.41×10^{-4}
		w^0	-5.03×10^{-1}
	$V_k(z)$	z^2	-3.60×10^{-2}
		z^1	-1.26×10^{-1}
		z^0	-4.41×10^{-1}
2	$U_k(w)$	w^1	6.38×10^{-4}
		w^0	-1.29×10^{-1}
	$V_k(z)$	z^2	1.45×10^{-1}
		z^1	-1.57×10^{-1}
		z^0	-7.26×10^{-2}

Table 4: Fitting parameters for truncated SVD polynomial fits for $\alpha,\gamma=\sum_{k=1}^{2}U_k(w)V_k(z)$ for $w=\log(1-\xi)$ and $z=\lambda^2$.